PCCP

Dynamic Article Links

Cite this: *Phys. Chem. Chem. Phys.*, 2011, **13**, 7666–7674

www.rsc.org/pccp

PAPER

A first principles study of water oxidation catalyzed by a tetraruthenium-oxo core embedded in polyoxometalate ligands†‡

Simone Piccinin*[ab] and Stefano Fabris[ab]

Received 23rd September 2010, Accepted 20th January 2011
DOI: 10.1039/c0cp01915a

We present a computational study addressing the catalytic cycle of a recently-synthesized all-inorganic homogeneous catalyst capable to promote water oxidation with low overpotential and high turnover frequency [Sartorel *et al.*, *J. Am. Chem. Soc.*, 2008, **130**, 5006; Geletii *et al.*, *Angew. Chem., Int. Ed.*, 2008, **47**, 3896]. This catalyst consists of a tetraruthenium-oxo core $[Ru_4O_4(OH)_2\cdot(H_2O)_4]^{6+}$ capped by two polyoxometalate $[SiW_{10}O_{36}]^{8-}$ units. The reaction mechanism underpinning its efficiency is currently under debate. We study a reaction cycle involving four consecutive proton-coupled electron transfer (PCET) processes that successively oxidize the four Ru^{IV}–H_2O units of the initial state (S_0) to the four Ru^{V}-OH centers of the activated intermediate (S_4). The energetics of these electrochemical processes as well as the structural and electronic properties of the reaction intermediates are studied with *ab initio* Density Functional Theory (DFT) calculations. After characterizing these reaction intermediates in the gas phase, we show that the solvated tetraruthenate core undergoes a solvent-induced structural distortion that brings the predicted molecular geometry to excellent agreement with the experimental X-ray diffraction data. The calculated electronic properties of the catalyst are instead weakly dependent on the presence of the solvent. The frontier orbitals of the initial state as well as the electronic states involved in the PCET steps are shown to be localized on the tetraruthenium-oxo core. The reaction thermodynamics predicted for the intermediate reaction steps is in good agreement with the available cyclic voltammetry measurements up to S_3, but the calculated free energy difference between the initial and the activated state (S_0/S_4) turns out to be significantly lower than the thermodynamic limit for water oxidation. Since the oxidizing power of the S_0/S_4 couple is not sufficient to split water, we suggest that promoting this reaction would require cycling between higher oxidation states.

1. Introduction

The ultimate goal of artificial photosynthesis is the conversion and storage of solar energy into high-energy chemical fuels. To this end, the oxidation of water leading to O_2 evolution is one of the limiting reaction steps.[1,2] This electrochemical semi-reaction involves the release of four electrons and four protons as well as the formation of an O–O bond:

$$2H_2O \rightarrow O_2 + 4H^+ + 4e^- [\Delta G(\mathrm{pH} = 0, \mathrm{NHE}) = 4.92\ \mathrm{eV}]. \quad (1)$$

Finding stable catalysts capable of promoting this reaction efficiently and with low overpotential is extremely challenging, and it is considered to be one of the key bottlenecks for the development of artificial photosynthetic devices. Several materials have been proposed in the past few years, including metal-oxide or semiconducting surfaces/nanoparticles (such as RuO_2,[3] IrO_2,[4] CoO_x)[5] as well as molecular organometallic catalysts based on Mn[6] and Ru[7] (for a review of the topic see ref. 8). Molecular catalysts are, in general, more efficient than metal oxides but they suffer from poor stability, since the organic ligands are quickly oxidized by the reaction intermediates, thus degrading their performance.[8] Here, the paradigmatic example is the "blue dimer", *cis*,*cis*-$[(bpy)_2(H_2O)RuORu(H_2O)(bpy)_2]^{4+}$, which is the best characterized molecular catalyst for water oxidation.[7]

A breakthrough in this field came in 2008, when two research groups independently reported the synthesis of an efficient fully inorganic catalyst for water oxidation. This is a Ru-based polyoxometalate (Ru_4–POM) molecule that is prepared as a salt and dissolves in water forming an anion with charge 10−. The Ru_4–POM complex, which is the

[a] *CNR-IOM DEMOCRITOS Theory@Elettra Group, Istituto Officina dei Materiali, s.s. 14 km 163.5 in Area Science Park, 34149 Trieste, Italy. E-mail: piccinin@sissa.it; Fax: +39 040-3758776; Tel: +39 040-3758737*
[b] *SISSA-Scuola Internazionale Superiore di Studi Avanzati and Italian Institute of Technology (IIT-SISSA Unit), via Bonomea 265, I-34136 Trieste, Italy*

† Electronic supplementary information (ESI) available. See DOI: 10.1039/c0cp01915a

‡ This article was submitted following the 1st workshop on Energy Materials, organised by The Thomas Young Centre, and held on 7–9 September 2010 at University College London.

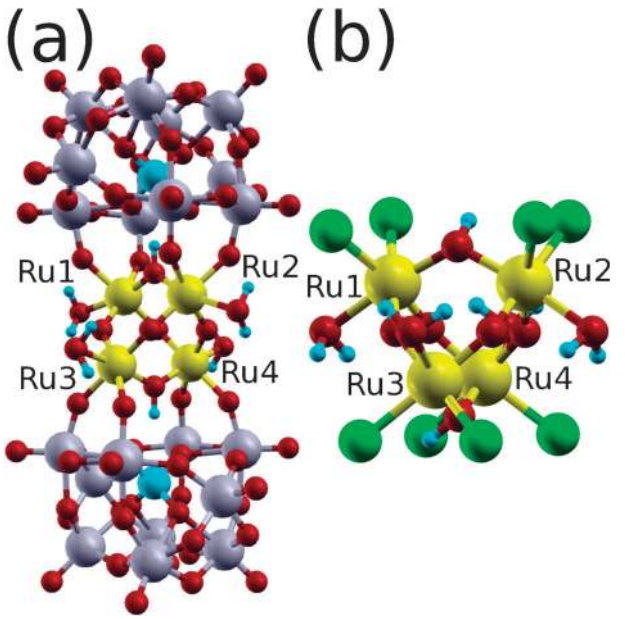

Fig. 1 Molecular structure for the initial state S_0 of the full Ru_4–POM complex (a) and of the simplified Ru_4–Cl model (b). Red, gray, small light blue, large light blue, yellow, and green spheres represent O, W, H, Si, Ru, and Cl atoms, respectively.

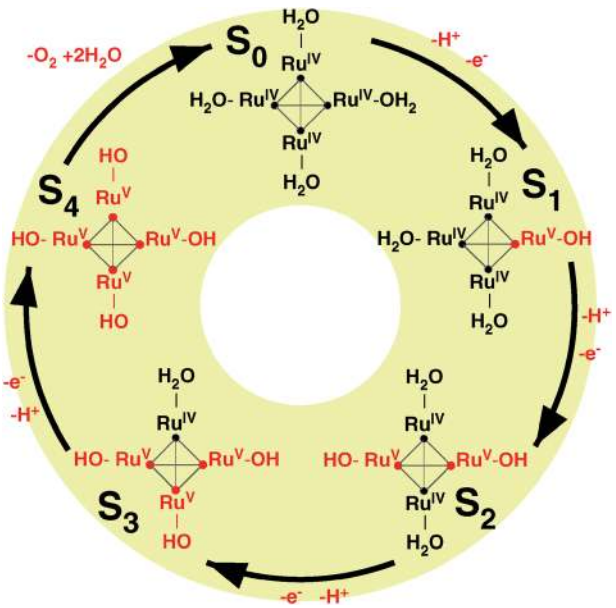

Fig. 2 Scheme of the catalytic cycle studied in this work, from the initial (S_0) to the activated (S_4) states, which are separated by four PCET events.

subject of the present study, catalyzes water oxidation with low overpotential (0.35 eV),[9] high turnover frequencies (>450 cycles per hour) and no deactivation,[10,11] making it one of the best catalysts for water oxidation reported to date. A stable oxygen-evolving anode based on this compound has been recently synthesized by depositing the Ru_4–POM catalyst on a conducting substrate of functionalized carbon nanotubes.[9]

The structure of the Ru_4–POM anion was determined experimentally by means of X-ray crystallography on molecular crystals.[10,11] Its active core is formed by four Ru atoms at the vertices of a tetrahedron (see Fig. 1) which are linked by six bridging O atoms forming two μ-hydroxo and four μ-oxo bridges. Each Ru atom is proposed to be in a Ru^{IV} (d^4) oxidation state and binds a water molecule. The resulting tetraruthenate $[Ru_4(\mu\text{-}O)_4(\mu\text{-}OH)_2(H_2O)_4)]^{6+}$ core is capped, on each side, by a $[\gamma\text{-}SiW_{10}O_{36}]^{8-}$ polyoxometalate, thus leading to the Ru_4–POM anion, which has a 10− charge and D_{2d} symmetry. The Ru tetrahedron is slightly distorted, with Ru–Ru distances in the 3.47–3.66 Å range. Following the nomenclature introduced by Sartorel *et al.*,[10] we will refer to this initial structure as S_0, which has already been the focus of some theoretical investigations.[12,13]

The catalytic cycle investigated in this work was proposed on the basis of Raman spectroscopy[12] and is schematically displayed in Fig. 2. During this cycle, the initial state S_0 (comprising four Ru^{IV}-H_2O units) is transformed to the active state S_4 (comprising four Ru^{V}-OH units) by four successive PCET processes. In each PCET step the water molecule bound to a Ru center loses a proton with the concomitant oxidation of one ruthenium atom from Ru^{IV} to Ru^{V}. The S_4 state has been proposed to be the catalytically active species promoting the oxidation of water. This reaction mechanism is also consistent with the dependency of the cyclic voltammetry on the pH (~0.59 meV per pH unit).[14]

The goal of the present computational work based on Density Functional Theory (DFT) is to study the evolution of the Ru_4–POM complex during this catalytic cycle in which water is oxidized and molecular oxygen is evolved. We first characterize the structural and electronic properties of the initial state S_0 in the gas phase as well as its dynamics in the presence of a solvent (described explicitly). The characterization is then extended to all reaction intermediates S_1–S_4 of the catalytic cycle described above. The energetics of water oxidation is addressed in terms of these intermediates with the method proposed by Nørskov and coworkers[15]. Different sets of calculations employing the standard generalized gradient approximation (GGA) as well as hybrid functionals demonstrate the important role played by the exchange and correlation functional in yielding reliable computational predictions. The comparison between the calculated reduction potentials and the available experimental cyclic voltammograms is used to discuss this reaction mechanism in the context of other alternative reaction mechanisms proposed in the literature, most prominently the work of Geletii *et al.*[14]

2. Computational methods

2.1 Electronic structure calculations

The DFT calculations presented in this work were performed with the QUICKSTEP program[16] provided by the CP2K package.[17] This program uses an atom-centered Gaussian-type basis to represent the wave functions together with an auxiliary plane wave basis to describe the electronic density. The electron-ion interactions were modeled through the Goedecker–Teter–Hutter (GTH) pseudopotentials. The dependency of the results on the approximations for the

exchange and correlation (XC) functionals is determined by exploring the following functionals: the generalized gradient approximation (using the PBE functional),[18] as well as the B3LYP[19,20] and the HSE06[21] hybrid functionals.

Since PCET reactions involve the removal of a H atom from the H_2O molecules coordinated to the Ru atoms, we have performed a preliminary study for testing the dependency of the computed quantities on the choice of the basis set for the O and H atoms. To this end, we considered six different Gaussian-type basis sets for the O and H atoms, namely DZVP, TZVP, TZV2P, aug-TZV2P, aug-QZV2P and aug-TZV2P-MOLOPT (DZV, TZV, QZV stand for double-, triple-, and quadruple-ζ valence functions, P and 2P indicate that one or two polarization functions have been included, and aug- indicates the inclusion of diffuse functions). This analysis was performed on a simplified model of the Ru_4–POM molecule (defined in the following section) in the initial S_0 and final S_4 states of the catalytic cycle. The results obtained with the different basis sets are reported in the ESI† and include (i) the Ru–Ru and Ru–H_2O distances, (ii) the Mulliken charges on the Ru atoms, and (iii) the corresponding spin densities. On the basis of this analysis, we conclude that the aug-TZV2P (for O and H), DZVP-MOLOPT (for Ru, W and Si), and the DZVP (for Cl) basis sets ensure sufficiently converged results for distances, spin densities and Mulliken charge differences. All the results reported in the following were obtained with these basis sets. The cutoff for the plane wave representation of the charge density was set to 280 Ry.

Unrestricted spin-polarized calculations were always employed, investigating, for every structure, solutions with total magnetization $M = 2S + 1 = 1,3,5,7$ for structures with an even number of electrons, and $M = 2S + 1 = 2,4,6$ for structures with an odd number of electrons. Where relevant, both the ferromagnetic (FM) and antiferromagnetic (AF) couplings between the Ru atoms were explored.

2.2 Structural models

Besides the full polyoxometalate Ru_4–POM anion described above (charge 10−, Fig. 1), we also considered a simplified model structure in which the $[\gamma\text{-}SiW_{10}O_{36}]^{8-}$ polyoxometalate units are replaced by four Cl^- ions, while leaving the $[Ru_4(\mu\text{-}O)_4(\mu\text{-}OH)_2(H_2O)_4)]^{6+}$ core unchanged. This substitution leads to the formation of an anion with charge 2−, which will be denoted in the following as Ru_4–Cl. The latter structure was employed to reduce the computational cost of some selected calculations, similarly to previous studies.[12] All structures were relaxed until the forces acting on each atom were below 4.5×10^{-4} a.u. (0.023 eV $Å^{-1}$).

2.3 QM/MM simulations and representation of the solvent

The influence of the liquid environment on the structural and electronic properties of the Ru_4–POM molecule was described by an explicit atomistic description of the solvent. We employed the QM/MM approach as implemented in the CP2K package,[22] where a portion of the whole system (Ru_4–POM in our case) is described at the quantum-mechanical (*i.e.* DFT) level, while the remaining part of the system (the solvent) is treated at the molecular-mechanics level, using a classical force field. Water was modeled with the TIP3P model,[23] and charge neutrality was maintained by including 10 Na^+ counterions. Besides the electrostatic interaction, the Ru_4–POM and the TIP3P water molecules interact also *via* a Lennard-Jones (LJ) potential. Since the outer surface of the POM caps comprises of oxygen atoms, we limited the interaction of the POM with the solvent to these exposed O atoms only. In particular, their interaction with the TIP3P water molecules and Na^+ counterions was modeled with the same LJ parameters of the oxygens in the TIP3P model.

The dimensions of the simulation cell were $34.20 \times 34.20 \times 45.60$ Å, including 1822 TIP3P water molecules. The size of the system was determined so that the excess of negative charge on the Ru_4–POM anion is effectively screened by the solvent. This cell size was therefore determined by preliminary molecular dynamics (MD) runs with a purely classical force field in the NPT ensemble at zero pressure. After determining the appropriate cell size, we run an additional MD simulation of $\sim$1 ns in the NVT ensemble at room temperature with the purely classical force field to equilibrate the system.

The QM/MM simulation consisted in a molecular dynamics run in the NVT ensemble, using the Nosé–Hoover thermostat to enforce a constant temperature of 300 K. After a $\sim$0.5 ps equilibration run we run a $\sim$1.5 ps MD monitoring the structural and electronic properties of the Ru_4–POM. The electronic structure properties reported in Section 3.2 were extracted from single point calculations at selected snapshots along the MD simulation.

2.4 Calculation of the energetics of the catalytic cycle

The thermochemistry of the water oxidation reaction was studied by focusing on the free energy differences between the intermediates S_0–S_4. The thermodynamics of the catalytic cycle was studied with the protocol proposed by Nørskov *et al.*[15], which has been already applied to the study of water oxidation[24–26] and oxygen reduction[15] reactions on metal and metal-oxide surfaces. Since this method has been already presented, applied and reviewed,[27] in the following we give only a very a brief description of the important concepts. In this framework, the possible energy barriers separating the reaction intermediates are not addressed, therefore the kinetic processes by which electrons and protons are extracted from the Ru_4–POM molecule will not be investigated.

Since all the events considered here are PCET, we do not need to compute separately the chemical potentials of H^+ and e^-, but simply the chemical potential of the pair. By setting the zero-reference of the free energy to the normal hydrogen electrode (NHE), defined by the equilibrium

$$H^+ + e^- \leftrightarrow 1/2H_2, \tag{2}$$

the free energy of the pair $H^+ + e^-$ is equal to half the free energy of a hydrogen molecule at standard conditions. At zero bias potential and at pH = 0, the free energy change ΔG of a reaction is computed as

$$\Delta G = \Delta E + \Delta ZPE + \Delta H - T\Delta S, \tag{3}$$

where ΔE is the difference of the DFT total energies, ΔZPE is the change in zero point energy, computed using the DFT

Table 1 Zero point energy difference (ΔZPE) and enthalpic plus entropic contribution to the free energy change ($\Delta H - T\Delta S$) for the intermediates S_i of the catalytic cycle

State	ΔZPE	$\Delta H - T\Delta S$
S_0	0.00	0.00
S_1	−0.23	−0.16
S_2	−0.46	−0.32
S_3	−0.68	−0.47
S_4	−0.91	−0.63

vibrational frequencies, ΔH and ΔS are the changes in enthalpy and entropy, computed using standard thermodynamic tables.[28] The zero-point energy changes between intermediates separated by a PCET event are calculated with a normal mode analysis of the S_0 and S_1 states as well as of the H_2 molecule: $\Delta ZPE(S_1) = ZPE(S_1) + 1/2ZPE(H_2) - ZPE(S_0)$. These quantities, reported in Table 1, are evaluated at the PBE/TZV2P level and we assume that each PCET reaction leads to the same ΔZPE contribution. The change in entropy ΔS associated with the release of a proton and an electron is, by virtue of eqn (2), equal to half the entropy of a hydrogen molecule at standard conditions, *i.e.* 0.21 eV. Similarly, the release of a proton and an electron leads to a change in enthalpy of 0.05 eV.

3. Results and discussion

3.1 Initial state S_0: isolated molecule

In this Section we investigate the structural and electronic properties of the initial state S_0. The limit of the isolated molecule in the gas phase is used as a reference, both for establishing the predictions of different energy functionals, as well as for determining the changes induced by the interaction with the solvent (reported in the following Section).

3.1.1 Full Ru_4–POM complex. The equilibrium geometry of the gas-phase Ru_4–POM molecule in the initial state S_0 (Fig. 1a) was determined starting from the experimental coordinates. The Ru–Ru interatomic distances resulting from the PBE functional (PBE/full in Table 3) are in fair agreement with the experimental values but do not capture the structural distortion of the tetraruthenium-oxo core. In the gas phase, the Ru–Ru distances are almost degenerate (3.53–3.56 Å), while XRD data show that the μ-hydroxo bridge (3.66 Å) is longer than the μ-oxo one (3.47 Å). We anticipate that this distortion is correctly predicted only when the molecule is solvated in solution. As shown in Section 3.2, by accounting for the solvent effects, the same PBE functional yields an excellent agreement with the experimental structure of the tetraruthenium-oxo core.

The PBE/full calculations predict an open-shell singlet ground state for S_0, in agreement with the experimental evidence that it is a diamagnetic, EPR silent, state.[11,12] According to the Mulliken population analysis, there is an excess of positive charge (0.55e) on each Ru atom. These atoms are antiferromagnetically coupled across the μ-hydroxo bridge, as shown by the atomic spin polarization (difference between spin up and spin down densities on the Ru atoms) reported in Table 2. The calculated density of electronic states (DOS) is displayed in Fig. 3a together with the projections (PDOS) on the POM (red) and tetraruthenium-oxo core (black). These PDOS clearly show that the frontier orbitals belong to the core while the electronic states of the POM ligands start appearing at energies ∼1 eV above/below the HOMO/LUMO levels. The calculated PBE HOMO/LUMO gap is 0.39 eV. The four intermediates in the catalytic cycle involve removing four electrons from the four highest occupied orbitals of this S_0 state. The energies of these orbitals lie in a 0.10 eV window therefore forming a quasi-continuum, in agreement with the findings of Quiñonero *et al.*[13]

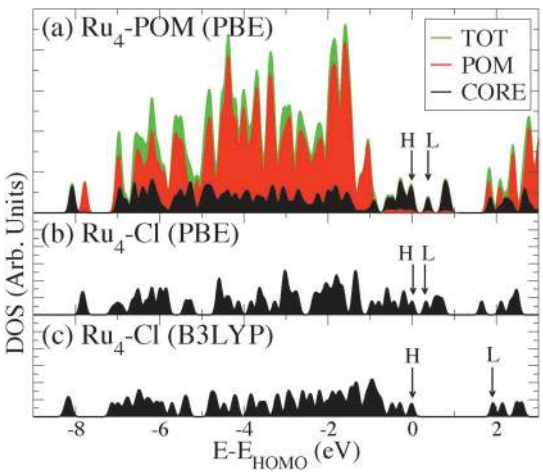

Fig. 3 Total (green), and partial density of states projected on the tetraruthenium-oxo core (black) and on the polyoxometalate ligands (red). (a) Ru_4–POM molecule at the PBE level, (b) Ru_4–Cl model at the PBE and (c) B3LYP levels. H and L indicate the HOMO and LUMO, respectively.

Table 2 Differences of up and down Mulliken spin density (μ) localized on the Ru atoms for the various intermediate states S_i. In each block, the two elements in the first row are μ(Ru1) and μ(Ru2), while the two elements in the second row are μ(Ru3) and μ(Ru4). PBE/full refers to the calculation done on the full Ru_4–POM model, while all other calculations have been performed on the simplified Ru_4–Cl model. *M* indicates the multiplicity

Functional	Ru atoms	$S_0(M = 1)$	$S_1(M = 2)$	$S_2(M = 3)$	$S_3(M = 2)$	$S_4(M = 1)$
PBE/full	μ(Ru1), μ(Ru2)	−0.48, 0.30	0.35, 0.87	1.28, 1.28	−1.37, −0.24	1.42, 1.46
	μ(Ru3), μ(Ru4)	−0.30, 0.48	0.20, −0.78	−0.68, −0.65	0.94, 1.30	−1.47, −1.41
PBE	μ(Ru1), μ(Ru2)	−0.69, 0.33	0.35, 0.69	1.11, 1.32	−1.33, −0.24	1.41, 1.34
	μ(Ru3), μ(Ru4)	−0.35, 0.72	0.47, −0.83	−0.12, −1.04	0.85, 1.40	−1.38, −1.38
B3LYP	μ(Ru1), μ(Ru2)	1.43, 1.41	1.39, 1.89	1.94, 1.94	1.86, 1.85	1.87, 1.90
	μ(Ru3), μ(Ru4)	−1.40, −1.43	−1.36, −1.32	−1.35, −1.37	−1.76, −1.31	−1.89, −1.88
HSE06	μ(Ru1), μ(Ru2)	1.48, 1.44	1.43, 1.95	2.00, 1.98	1.92, 1.91	1.94, 1.94
	μ(Ru3), μ(Ru4)	−1.46, −1.48	−1.40, −1.37	−1.41, −1.42	−1.84, −1.37	−1.94, −1.94

3.1.2 Validation of the simplified Ru_4–Cl model. The full Ru_4–POM molecule is computationally very demanding for calculations employing hybrid functionals, which have instead been performed on the simplified Ru_4–Cl model (Fig. 1b). We validate this structural simplification by showing that the overall structural and electronic properties predicted by the PBE functional are preserved by substituting the POM ligands with Cl^- ions (Ru–Ru and Ru–H_2O distances in Table 3). The ground state turns out to be a singlet also for the Ru_4–Cl model, with the same antiferromagnetic coupling of the full Ru_4–POM complex. The Mulliken population analysis gives a 0.47e positive charge on each of the four Ru atoms. The calculated DOS is shown in Fig. 3b. The main electronic features resemble those of the tetraruthenium-oxo core in the full Ru_4–POM molecule (Fig. 3a), with a HOMO–LUMO gap of 0.33 eV. These findings show that the structural and electronic properties of the Ru_4–POM are well captured by the simplified Ru_4–Cl model, suggesting that this simplification can be used when the cost of the calculations becomes prohibitively large.

3.1.3 GGA *vs.* hybrid functionals and discussion. Coming now to hybrid functionals, the geometry of the S_0 state of the Ru_4–Cl model was optimized by using the aug-TZV2P basis set. With the B3LYP functional we find that the Ru–Ru distances are in the 3.51–3.59 Å range (3.49–3.56 Å using the HSE06 functional) and that the Ru–O_{water} average distance is 2.23 (2.18) Å (see Table 3). Note that also these calculations do not predict the experimental structural distortion of the Ru tetrahedron cage. The ground state of S_0 is a singlet with FM coupling of the Ru atoms along the μ-hydroxo bridge (see Table 2). In this case the Mulliken population analysis places a 0.67 (0.61)e positive charge on the Ru atoms. The comparison between the DOS calculated at the PBE and B3LYP levels (Fig. 3b and c, respectively) shows a considerable increase in the HOMO–LUMO gap from 0.33 to 1.92 eV (1.65 with HSE06). The four highest occupied molecular orbitals lie, in this case, within a 0.29 (0.30) eV energy window. Overall, the inclusion of a portion of the Hartree–Fock exchange has the effect of localizing a higher spin density on the Ru atoms, while the geometry is only marginally affected. Most notably, the interaction between the spin densities localized on the Ru atoms across the μ-hydroxo bridge (*i.e.* the interaction between Ru1 and Ru2 and between Ru3 and Ru4, see Fig. 1) changes from AF in the case of PBE to FM in the case of hybrid functionals. We verified that the FM solution is favored over the AF one by 0.17 eV in the B3LYP case, while in the PBE case it was not possible to converge to a FM solution.

The electronic structure of the Ru centers can be interpreted on the basis of the ligand field theory. Each Ru ion is at the center of a distorted octahedron whose field splits the energy of the Ru-d orbitals in the t_{2g} and e_g levels, with two of them unpaired. The calculated spin polarization of about 1.5e (see Table 2) is consistent with a $Ru^{IV}(d^4)$ ion, having formally four electrons in the t_{2g} level.

3.2 Initial state S_0 in solution: QM/MM simulations

In this Section we investigate the changes induced by the solvent on the structural and electronic properties of the initial state S_0. The liquid environment was modeled by employing an explicit description of the water molecules and counterions, as described in Section 2.3. Given the high computational cost, the calculations were performed at the PBE/DZVP-MOLOPT level. We report in the included ESI† that this level of theory yields a sufficiently accurate description of the Ru–H_2O bond (see Tables I and II in the ESI†).

The Ru–Ru distances in the tetrahedron core during the MD simulation (~1.5 ps) are reported in Fig. 4. The effect of the solution is to differentiate the Ru–Ru distances, shortening those across the μ-oxo bridges (dashed lines) and increasing those across the μ-hydroxo bridges (continuous lines). With respect to the gas-phase geometry, the Ru_4O_6 core in solution undergoes a structural distortion leading to calculated Ru–Ru average distances (3.49 Å across the μ-oxo bridges and 3.67 Å across the μ-hydroxo bridges) that are in very good agreement with the experimental values (3.47 and 3.66 Å).

Quite interestingly, the distortion pattern described above is preserved during the whole dynamics (see Fig. 4) and is predicted also by a continuum dielectric model of the solvent.[13]

Table 3 Distances among Ru atoms in the Ru_4O_6 core of the intermediate states evaluated using the PBE, B3LYP and HSE06 functionals. PBE/full refers to the calculations performed on the full Ru_4–POM molecules, while all other calculations have been performed on the simplified Ru_4–Cl model. Bold labels refer to the Ru atoms oxidized from Ru^{IV} to Ru^V

State	Atoms	PBE/full	PBE	B3LYP	HSE06	Exp.
S_0	*d*(Ru1,Ru2)	3.53	3.58	3.59	3.56	3.66
	d(Ru3,Ru4)	3.54	3.57	3.57	3.55	3.66
	d(Ru1,Ru3)	3.54	3.54	3.56	3.51	3.47
	d(Ru1,Ru4)	3.56	3.50	3.53	3.52	3.48
	d(Ru2,Ru3)	3.56	3.49	3.51	3.49	3.47
	d(Ru2,Ru4)	3.54	3.53	3.54	3.53	3.46
	$\bar{d}$[(Ru–H_2O)	2.27	2.27	2.23	2.18	
S_1	*d*(**Ru1**,Ru2)	3.64	3.66	3.71	3.64	
	d(Ru3,Ru4)	3.54	3.58	3.55	3.55	
	d(**Ru1**,Ru3)	3.52	3.52	3.59	3.55	
	d(**Ru1**,Ru4)	3.60	3.54	3.59	3.57	
	d(Ru2,Ru3)	3.56	3.52	3.55	3.53	
	d(Ru2,Ru4)	3.58	3.47	3.56	3.55	
	$\bar{d}$(Ru–H_2O)	2.29	2.23	2.21	2.16	
	$\bar{d}$[(Ru–OH)	1.95	1.93	1.92	1.90	
S_2	*d*(**Ru1**,**Ru2**)	3.74	3.81	3.85	3.80	
	d(Ru3,Ru4)	3.54	3.58	3.53	3.51	
	d(**Ru1**,Ru3)	3.58	3.52	3.57	3.54	
	d(**Ru1**,Ru4)	3.60	3.56	3.56	3.53	
	d(**Ru2**,Ru3)	3.58	3.53	3.61	3.57	
	d(**Ru2**,Ru4)	3.60	3.55	3.55	3.54	
	$\bar{d}$[(Ru–H_2O)	2.28	2.22	2.21	2.16	
	$\bar{d}$(Ru–OH)	1.96	1.95	1.93	1.90	
S_3	*d*(**Ru1**,**Ru2**)	3.84	3.78	3.81	3.73	
	d(**Ru3**,Ru4)	3.69	3.69	3.71	3.63	
	d(**Ru1**,**Ru3**)	3.57	3.66	3.58	3.57	
	d(**Ru1**,Ru4)	3.58	3.57	3.59	3.58	
	d(**Ru2**,**Ru3**)	3.58	3.53	3.60	3.58	
	d(**Ru2**,Ru4)	3.49	3.49	3.63	3.54	
	$\bar{d}$[(Ru–H_2O)	2.34	2.24	2.23	2.19	
	$\bar{d}$(Ru–OH)	1.96	1.93	1.92	1.89	
S_4	*d*(**Ru1**,**Ru2**)	3.81	3.86	3.83	3.80	
	d(**Ru3**,**Ru4**)	3.83	3.84	3.85	3.80	
	d(**Ru1**,**Ru3**)	3.58	3.58	3.62	3.57	
	d(**Ru1**,**Ru4**)	3.60	3.57	3.61	3.58	
	d(**Ru2**,**Ru3**)	3.58	3.56	3.60	3.57	
	d(**Ru2**,**Ru4**)	3.58	3.57	3.61	3.55	
	$\bar{d}$[(Ru–H_2O)	—	—	—	—	
	$\bar{d}$(Ru–OH)	1.95	1.95	1.92	1.90	

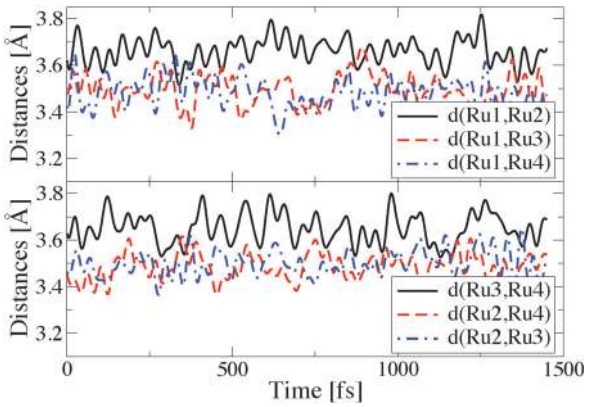

Fig. 4 Time evolution of the Ru–Ru distances during the QM/MM molecular dynamics simulation. In the top panel we consider one of the two pairs of Ru atoms linked by the μ-hydroxo bridge (Ru1 and Ru2) and two of the four pairs linked by the μ-oxo bridge (Ru1 and Ru3, Ru1 and Ru4). The remaining pairs are shown in the bottom panel.

By examining five snapshots of the MD run through single point calculations and comparing them with the results obtained in vacuum, we found that the electronic structure of the Ru_4–POM molecule is only weakly perturbed by the presence of the solvent. As an example, the HOMO–LUMO gap is in all cases between 0.30 and 0.40 eV (0.39 eV in vacuum) and the Ru atoms are antiferromagnetically coupled along the μ-hydroxo bridge as in the gas-phase calculation.

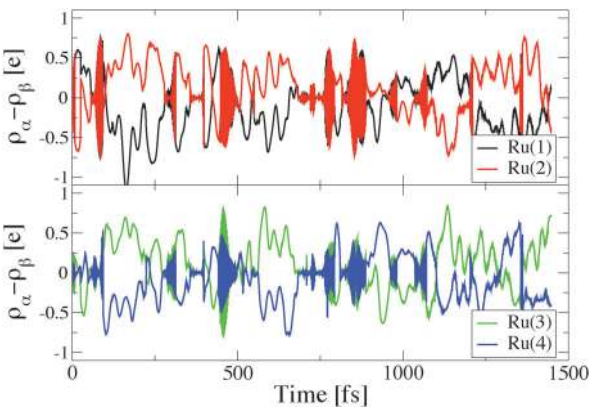

Fig. 5 Time evolution of the difference between the spin-up and spin-down Mulliken populations localized (spin density) on the Ru atoms during the QM/MM molecular dynamics simulation. The top (bottom) panel shows the spin density for Ru1 and Ru2 (Ru3 and Ru4), the top (bottom) pair connected by the μ-hydroxo bridge in Fig. 1. Notice how both pairs remain AF coupled along the dynamics.

By monitoring the time evolution of the atomic spin density on the four Ru atoms (Fig. 5) we can see that the antiferromagnetic coupling of these Ru pairs is preserved during the dynamics, while the magnitude and the sign of the atomic spin density on each Ru atom strongly fluctuates. There is an almost perfect antisymmetric correlation between the fluctuations of the spins of the atoms connected by the μ-hydroxo bridge, so as to preserve the antiferromagnetic coupling.

3.3 Reaction intermediates S_1–S_4

Having characterized the initial state, we now present the structural and electronic properties of the reaction intermediates S_1–S_4 (Fig. 6), with the goal of identifying the main changes induced by the four PCET steps during the catalytic cycle.

3.3.1 S_1. The intermediate complex S_1 is formed by removing a H atom from one of the water molecules coordinated to the Ru_4O_6 core. The minimum-energy structure is displayed in Fig. 6a, where an ellipse marks the hydroxyl group resulting from the PCET process. This process leads to the formation of an electron hole that formally oxidizes the Ru atom neighboring the hydroxyl ligand from Ru^{IV} to Ru^{V}. All functionals (GGA and hybrid) and model systems (Ru_4–POM and Ru_4–Cl) display an increase of the Mulliken charge associated with the oxidized Ru atom (Ru1) with respect to the value in the initial state. The increase is more prominent for the hybrid functionals (0.08–0.11e) than for the PBE one (0.06e). Note that the actual calculated values are quite different for the PBE (from 0.47 in S_0 to 0.53 in S_1) and for the hybrid functionals (from 0.68/0.62 in S_0 to 0.76/0.73 in S_1 for B3LYP/HSE06), the latter obviously predicting a higher localization of the hole on the metal centers.

The atomic spin densities predicted by the hybrid functional calculations fully support the oxidation of the Ru1 ion to Ru^{V} (Table 2). The increase of its spin density is consistent with the removal of one electron from the spin minority in the t_{2g} level, resulting, formally, in three unpaired electrons at the Ru^{V} atom. This is precisely the case requiring a reliable description of the localization of the electron hole, something in which the hybrid functionals are known to be better suited than the traditional gradient corrected ones, in which the self-interaction error is major. Indeed, the PBE electronic solution cannot support the same ligand field model of the Ru^{V}–OH group.

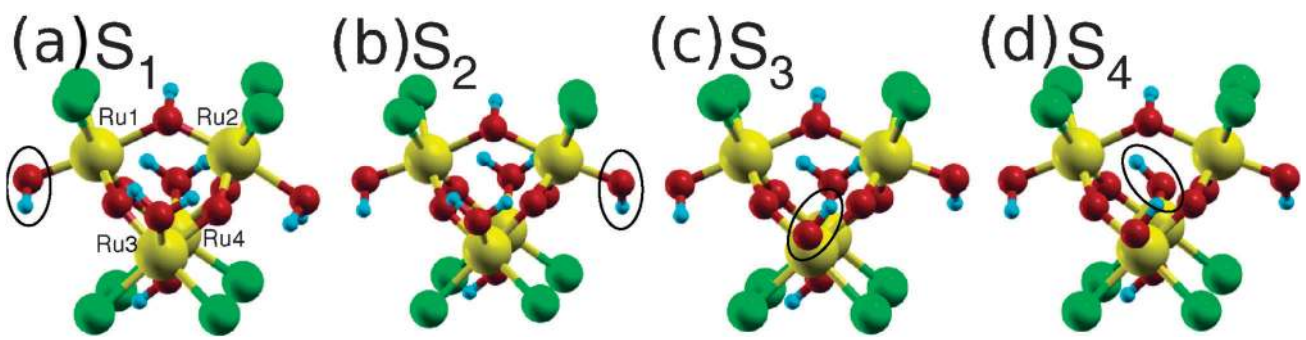

Fig. 6 S_1–S_4 intermediates of the catalytic cycle studied in this work. The ellipse indicates the hydroxyl group formed after every PCET step.

We can anticipate (as demonstrated in the following Section) that this inability of the GGA functionals to cancel the self-interaction strongly affects their reliability in capturing the energetics of the catalytic cycle.

The larger positive charge localized on the oxidized Ru^V atom can be expected to drive apart its Ru^{IV} neighbors. Indeed, the increase of the Ru^V–Ru^{IV} distances can be clearly seen across the μ-hydroxo bridge (by about 0.08–0.12 Å), while the distances across the μ-oxo bridges are modified to a smaller degree (by 0.00–0.08 Å), as shown in Table 3. The geometries of the other bridges not involving the Ru^V center are instead scarcely affected (bond lengths change by less than 0.02 Å). The structural changes after the first PCET process can therefore be rationalized on the basis of an ionic model of the Ru-oxo core, in which the larger ionic charge localized on the oxidized Ru^V center drives the distortion of the tetrahedron. In agreement with this electrostatic interpretation, hybrid functionals predict a higher positive charge at the oxidized Ru atom than the gradient corrected one, and a correspondingly larger increase of the Ru^V–Ru^{IV} distance.

3.3.2 S_2. A second PCET step, in which a H atom is removed from the water molecule bound to Ru2, leads to the intermediate S_2 displayed in Fig. 6b. Also in this case the oxidation of Ru1 and Ru2 from Ru^{IV} to Ru^V is supported by the increase of their Mulliken positive charge to 0.59e at the PBE level (0.79 and 0.73 with the B3LYP and HSE06 functionals, respectively). This is accompanied by the increase of their atomic spin densities (Table 2) on the two oxidized Ru atoms, resulting, formally, from three unpaired electrons on the t_{2g} levels. The PBE solution is consistent with the prediction of the hybrid functionals, but with smaller magnitude of the atomic spin densities.

The change in the molecular structure follows the ionic model presented for the case of S_1, with a further increase of the Ru1–Ru2 distance from 3.66–3.71 Å in S_1 to 3.81–3.85 Å in S_2, due to the additive repulsive effect of the excess positive charge induced by the oxidation.

3.3.3 S_3. In the case of the S_3 intermediate (Fig. 6c) there is only one Ru^{IV} center (Ru4) bound to a water molecule, the others being in their oxidation state V and coordinated by a hydroxyl ligand. The average Mulliken charge on the oxidized Ru^V ions is compatible with the one presented for the previous cases, 0.55/0.75/0.70e with the PBE/B3LYP/HSE06 functionals, with the corresponding values for the Ru^{IV} center (Ru4) being 0.50/0.69/0.63e, respectively. As expected, the Ru1–Ru2 distance (*i.e.* the distance between two Ru^V atoms across the μ-hydroxo bridge) is larger than the Ru3–Ru4 one (*i.e.* the distance between a Ru^{IV} and a Ru^V atom across the μ-hydroxo bridge), in line with what seen for the previous intermediates (Table 3).

The interpretation of the atomic spin densities on the basis of the simple model applied to the previous intermediates does hold also for S_3 (Table 2). Starting from the S_2 solution, which displays two unpaired spins in the Ru^{IV} atoms and three unpaired spins in the Ru^V atoms, the oxidation of one Ru^{IV} atom leads to an increase of the corresponding atomic spin density (on Ru3, in our specific geometry), consistently with the removal of one electron from the minority spin of the Ru ion.

3.3.4 S_4. In the case of the S_4 intermediate, which is obtained from S_0 by replacing each of the four water molecules with OH groups (Fig. 6d), we find that, at the PBE level, the Ru–Ru distances along the μ-hydroxo bridges are both ~3.85 Å, while those along the μ-oxo bridges are ~3.57 Å (see Table 3). The tetrahedral structure of the Ru core is therefore significantly distorted compared to the S_0 state. The same behavior is displayed by hybrid functional calculations. The Mulliken charge on the four Ru atoms is 0.64e in the PBE calculation, 0.77e in the B3LYP calculation and 0.72e in the HSE06 one. By comparing these numbers with the corresponding ones for S_0 we see a clear increase of the positive charge localized at the Ru atoms upon their oxidation.

All three functionals give FM coupling between the Ru atoms across the μ-hydroxo bridge, with the hybrid functionals leading to a more localized atomic spin density. By comparing the magnitude of these quantities with those of S_2 we see that each of the four Ru^V atoms of S_4 has an atomic spin density comparable to that of the two Ru^V atoms of S_2, and higher than of the two Ru^{IV} atoms. This is consistent with our model in which the oxidation of all Ru atoms leads to three unpaired electrons in the t_{2g} level of every Ru atom.

3.4 Energetics of the intermediate states of oxidation

In this section we present and discuss the free energies of the S_i intermediates. We do this by using the methodology outlined in Section 2.4. The total energy differences ΔE in eqn (3) are evaluated through DFT calculations of the S_i intermediates in vacuum, which have been characterized in the previous Section. We note that this is an acceptable approximation since solvent effects on these thermodynamic quantities have been shown to be negligibly small.[12] In particular, the main quantity of interest here is the energy difference between S_0 and S_4. The inclusion of an implicit solvent model modifies this quantity by just 0.05 eV.

3.4.1 Validation of the simplified Ru_4–Cl model. Before describing the thermochemistry of the PCET reactions transforming S_0 into S_4 (Fig. 2), we first assess that the thermodynamics calculated for the simplified Ru_4–Cl model correctly reproduces the one of the full Ru_4–POM complex. To this end, we calculate the total energy difference

$$\Delta E(S_i) = E(S_i) + \frac{i}{2}E(H_2) - E(S_0) \qquad (4)$$

between the state S_i and the state S_0 for the Ru_4–Cl and Ru_4–POM systems. The data are reported in Table 4 (third and fourth columns) and demonstrate that, at the PBE level the two models agree within 0.1 eV per PCET event.

3.4.2 Total energy differences. In the mechanism under analysis, the structures of the intermediates S_i differ only by the number of H atoms in the ligands of the four Ru centers. Therefore the POM capping units remain almost invariant during the catalytic cycle. We have established, in agreement with the findings of Quiñonero *et al.*,[13] that the frontier orbitals are strongly localized on the tetraruthenium-oxo core

Table 4 Relative energies of the S_i intermediates, computed using three different types of XC functionals (PBE, HSE06, B3LYP) and the aug-TZV2P basis set. The HSE06 and B3LYP results are obtained using the relaxed geometries at the DZVP level, while the PBE results are fully relaxed at the aug-TZV2P level. In the case of hybrid functionals, ΔE_{Ru_4-Cl} is used to estimate ΔE_{Ru_4-POM} (see text). *M* indicates the multiplicity and all energies are in eV

State	*M*	$\Delta E^{PBE}_{Ru_4-Cl}$	$\Delta E^{PBE}_{Ru_4-POM}$	$\Delta E^{B3LyP}_{Ru_4-Cl}$	$\Delta E^{B3LyP}_{Ru_4-POM}$	$\Delta E^{HSE06}_{Ru_4-Cl}$	$\Delta E^{HSE06}_{Ru_4-POM}$
S_0	1	0.00	0.00	0.00	0.00	0.00	0.00
S_1	2	1.00	1.03	1.06	1.09	1.25	1.28
S_2	3	2.13	1.92	2.56	2.35	2.87	2.66
S_3	2	3.24	3.02	3.90	3.68	4.33	4.11
S_4	1	4.39	4.04	5.27	4.92	5.89	5.54

(Fig. 3). These considerations indicate that also the free energy differences between PCET steps, ΔG_{Ru_4-POM}, will be mostly determined by local changes (structural and electronic) in the tetraruthenium-oxo core. Hence, the energetics of the full Ru_4–POM complex, ΔE_{Ru_4-POM}, can be estimated on the basis of the accurate energy differences calculated with the hybrid functionals in the Ru_4–Cl model, ΔE_{Ru_4-Cl}, corrected for the small contribution of the POM ligands calculated at the PBE level:

$$\Delta E^{HSE06}_{Ru_4-POM}(S_i) \simeq \Delta E^{HSE06}_{Ru_4-Cl}(S_i) + \Delta E^{PBE}_{Ru_4-POM}(S_i) - \Delta E^{PBE}_{Ru_4-Cl}(S_i), \quad (5)$$

(and analogous for the B3LYP functional). This approximation allows us to relate the thermodynamics calculated for the small Ru_4–Cl model to the experimental data measured for the molecular complex in solution.

The cost of each PCET step, and the first one in particular, turns out to be smaller with the PBE than with hybrid functionals (see Table 4). This can be rationalized by the different descriptions of the Ru–OH bond provided by different functionals, which can already be seen for a model system consisting of one Ru atom undergoing the Ru–H_2O/Ru–OH transition (see ESI†, Table III).

3.4.3 Thermodynamics of the catalytic cycle. We report in Table 5 the values of the free energy differences ΔG_{Ru_4-POM} for the intermediates S_i evaluated with the three functionals, together with the corresponding experimental values obtained from the cyclic voltammetry measurements[12] (referenced to pH = 0). Note that these measurements could not identify a clear peak corresponding to the S_3/S_4 pair and therefore the experimental value for $\Delta G(S_0 \rightarrow S_4)$ is not known. We start by comparing the computed thermodynamics with the available experimental data, *i.e.* the S_0/S_3 couple. Overall, the hybrid functionals yield a good agreement with experiment, with errors in the free energy after three PCET steps below 0.25 eV (7/9% at the B3LYP/HSE06 level). In turn, this reaction thermodynamics exposes the limits of the PBE functional, which is affected by important discrepancies with the experiment, as large as 0.81 eV (31%).

The experimental trend of a slight increase in the cost of a PCET as a function of the oxidation step, 0.76/0.88/1.07 eV for $\Delta G(S_0 \rightarrow S_1)/\Delta G(S_1 \rightarrow S_2)/\Delta G(S_2 \rightarrow S_3)$, respectively, is qualitatively reproduced by both B3LYP (0.70/0.87/0.96 eV) and HSE06 (0.89/0.99/1.08 eV). We note however that the fourth oxidation step in both cases (0.85/1.04 eV) does not follow this trend.

Table 5 Free energies of the S_i intermediates, computed using three different types of XC functionals (PBE, B3LYP, HSE06) and the aug-TZV2P basis set. The quantity $\Delta G(S_i)$ is defined as $G(S_i) + i/2G(H_2) - G(S_0)$, where $i = \{0,4\}$. The unit of all energies is eV

State	$\Delta G^{PBE}_{Ru_4-POM}$	$\Delta G^{B3LyP}_{Ru_4-POM}$	$\Delta G^{HSE06}_{Ru_4-POM}$	Expt.[12]
S_0	0.00	0.00	0.00	0.00
S_1	0.64	0.70	0.89	0.76
S_2	1.14	1.57	1.88	1.64
S_3	1.87	2.53	2.96	2.71
S_4	2.50	3.38	4.00	—

According to the catalytic cycle under analysis, water oxidation is promoted by the S_4 intermediate. To achieve this goal, the free energy difference $\Delta G(S_0 \rightarrow S_4)$ has to exceed the thermodynamic limit of 4.92 eV. Clearly, our calculations show that the S_0/S_4 couple does not fulfill this requirement, since the computed values 3.38/4.00 eV (B3PLYP/HSE06) are by more than 0.9 eV below this thermodynamic limit. Given the overall good agreement with the experiment obtained for the S_0/S_3 couple, we expect a similarly high predictive power of the hybrid-functional calculations also for the S_0/S_4 energetics. The difference between the theoretically predicted S_0/S_4 couple and the thermodynamic value for water oxidation (0.9 eV) is much larger than the variations due to different approximations in the exchange and correlation functional ($\sim$0.4 eV for S_0/S_3). These calculations therefore show that the S_0/S_4 couple does not have enough oxidizing power to split water. On the basis of this result we suggest that promoting water oxidation would require higher oxidation states than those undertaken in the four PCET processes assumed in the present $S_0 \rightarrow S_4$ catalytic cycle.

One possibility for reaching the thermodynamic driving force necessary to promote water oxidation would be to further oxidize the catalyst. To do so, a catalytic cycle comprising four PCET processes would require the removal of H atoms from the hydroxyl ligands of the Ru^V ion, forming Ru^{VI}=O oxo or Ru^V–$O^\bullet$ oxyl groups. We note that this has important analogies with similar bimetallic Ru-based metal-organic catalysts.[29,30] Incidentally, for these systems, DFT calculations based on the B3LYP functional reproduced very well the available experimental energetics of the four-electron oxidation with errors below 0.3 eV.[31] Another possibility would be that some (or all) reaction intermediates were not related by PCET processes as assumed here but

rather by electron transfer steps. This would then modify the charge of the molecular complex during the cycle, something that has indeed been postulated to justify the approximately linear increase of the S_i/S_{i+1} redox potential measured by Geletii and coworkers.[14] We are currently validating the latter hypothesis with computational methods cabable of quantifying the screening effects of the solvent on differently charged Ru_4–POM anions.

4. Conclusions

In conclusion, we have investigated the structural, electronic, and thermodynamic properties of a Ru_4–POM molecular complex by means of DFT calculations.

The initial S_0 state is predicted to be in an open-shell singlet ground state, with a finite atomic spin density localized at the Ru atoms. The calculated Mulliken charges and spin polarization are compatible with $Ru^{IV}(d^4)$ ions with two unpaired electrons in the t_{2g} levels, AF coupled across the μ-hydroxo bridge. The QM/MM simulations of the solvated molecule show that the tetraruthenium-oxo core undergoes a solvent-induced structural distortion that brings the calculated average distances in excellent agreement with the experimental values.

Removing a hydrogen atom from one Ru^{IV}–H_2O unit of the core drives the oxidation of the Ru center to Ru^{V}–OH. This is supported by an increase of the Ru Mulliken charge (which determines an electrostatic-driven distortion of the Ru tetrahedron), and of the Ru spin polarization. We have also shown that the main features of the electronic structure changes underpinning the Ru^{IV}–H_2O/Ru^{V}–OH transformation can be inserted in the framework of ligand-field theory.

The free energy difference between the S_0 and S_3 states calculated with the hybrid functionals agrees within 0.25 eV with the corresponding experimental value. This is in line with the accurate thermodynamics predicted by these functionals for other Ru-based molecular complexes.[30] The same quantity predicted by the GGA/PBE functional is affected by discrepancies with experiment as large as 0.9 eV. The main result of our analysis is that the free energy difference between the initial state S_0 and the active state S_4 is significantly lower than the thermodynamical limit for water oxidation. This suggests that the S_0/S_4 couple is not the one responsible for the catalytic water splitting observed experimentally. One way to promote this reaction with four PCET processes would be a catalytic cycle involving higher oxidation states than the Ru^{IV}–H_2O/Ru^{V}–OH of the S_0/S_4 couple.

Acknowledgements

We are grateful to Giacinto Scoles for drawing our attention to this topic and to Andrea Sartorel and Marcella Bonchio for useful discussions. This work was partially supported by the EU through the FP7 Marie Curie IRG Program (Project H2OSPLIT, Grant PIRG04-GA-2008-239199). The DEISA Extreme Computing Initiative (DECI-6) is acknowledged for generous allocation of computational resources.

References

1 N. S. Lewis and D. G. Nocera, *Proc. Natl. Acad. Sci. U. S. A.*, 2006, **103**, 15729.
2 V. Balzani, A. Credi and M. Venturi, *ChemSusChem*, 2008, **1**, 26.
3 H. Kadowaki, N. Saito, H. Hishiyama, H. Kobayashi, Y. Shimodaira and Y. Inoue, *J. Phys. Chem. C*, 2007, **111**, 439.
4 T. Nakagawa, C. A. Beasley and R. W. Murray, *J. Phys. Chem. C*, 2009, **113**, 12958.
5 M. W. Kanan and D. G. Nocera, *Science*, 2008, **321**, 1072.
6 M. Yagi and K. Narita, *J. Am. Chem. Soc.*, 2004, **126**, 8084.
7 S. W. Gersten, G. J. Samuels and T. J. Meyer, *J. Am. Chem. Soc.*, 1982, **104**, 4029.
8 X. Sala, I. Romero, M. Rodrguez, L. Escriche and A. Llobet, *Angew. Chem., Int. Ed.*, 2009, **48**, 2842.
9 F. M. Toma, A. Sartorel, M. Iurlo, M. Carraro, P. Parisse, C. Maccato, S. Rapino, B. R. Gonzalez, H. Amenitsch, T. Da Ros, L. Casalis, A. Goldoni, M. Marcaccio, G. Scorrano, G. Scoles, F. Paolucci and M. Prato, *Nat. Chem.*, 2010, **2**, 826.
10 A. Sartorel, M. Carraro, G. Scorrano, R. D. Zorzi, S. Geremia, N. McDaniel, S. Bernhard and M. Bonchio, *J. Am. Chem. Soc.*, 2008, **130**, 5006.
11 Y. V. Geletii, B. Botar, P. Kögerler, D. A. Hillesheim, D. G. Musaev and C. G. Hill, *Angew. Chem., Int. Ed.*, 2008, **47**, 3896.
12 A. Sartorel, E. S. P. Miró, S. Romain, M. Carraro, G. Scorrano, M. D. Valentin, A. Llobet, C. Bo and M. Bonchio, *J. Am. Chem. Soc.*, 2009, **131**, 16051.
13 D. Quiñonero, A. L. Kaledin, A. E. Kuznetsov, Y. V. Geletti, C. Besson, C. L. Hill and D. G. Musaev, *J. Phys. Chem. A*, 2010, **114**, 535.
14 Y. Geletii, C. Besson, Y. Hou, Q. Yin, D. G. Musaev, D. Quinonero, R. Cao, K. I. Hardcastle, A. Proust, P. Kögerler and C. G. Hill, *J. Am. Chem. Soc.*, 2009, **131**, 17360.
15 J. K. Nørskov, J. Rossmeisl, A. Logadottir and L. Lindqvist, *J. Phys. Chem. B*, 2004, **108**, 17886.
16 G. Lippert, J. Hutter and M. Parrinello, *Theor. Chem. Acc.*, 1999, **103**, 124.
17 The CP2K developers group, http://cp2k.berlios.de/.
18 J. P. Perdew, K. Burke and M. Ernzerhof, *Phys. Rev. Lett.*, 1996, **77**, 3865.
19 A. D. Becke, *J. Chem. Phys.*, 1993, **98**, 5648.
20 P. Stephens, F. J. Devlin, C. F. Chabalowski and M. J. Frisch, *J. Phys. Chem.*, 1994, **98**, 11623.
21 A. V. Krukau, O. A. Vydrov, A. F. Izmaylov and G. E. Scuseria, *J. Chem. Phys.*, 2006, **125**, 224106.
22 T. Laino, F. Mohamed, A. Laio and M. Parrinello, *J. Chem. Theory Comput.*, 2005, **1**, 1176.
23 W. L. Jorgensen, J. Chandrasekhar, J. D. Madura, R. W. Impey and M. L. Klein, *J. Chem. Phys.*, 1983, **79**, 926.
24 J. Rossmeisl, A. Logadottir and J. K. Nørskov, *Chem. Phys.*, 2005, **319**, 178.
25 J. Rossmeisl, J. K. Nørskov, C. D. Taylor, M. J. Janik and M. Neurock, *J. Phys. Chem. B*, 2006, **110**, 21833.
26 J. Rossmeisl, Z.-W. Qu, H. Zhu, G.-J. Kroes and J. K. Nørskov, *J. Electroanal. Chem.*, 2007, **607**, 83.
27 A. Valdés and G.-J. Kroes, *J. Phys. Chem. C*, 2010, **114**, 1701.
28 D. stull and H. Prophet, *JANAF Thermochemical Tables*, U.S. National Bureau of Standards, Washington, DC, 2nd edn, 1971.
29 F. Liu, J. J. Concepcion, J. W. Jurss, T. Cardolaccia, J. L. Templeton and T. J. Meyer, *Inorg. Chem.*, 2008, **47**, 1727–1752.
30 X. Yang and M.-H. Baik, *J. Am. Chem. Soc.*, 2006, **128**, 7476–7485.
31 X. Yang and M.-H. Baik, *J. Am. Chem. Soc.*, 2004, **126**, 13222–13223.

